N Ordas et al.

Transmission electron microscopy and X-ray absorption spectroscopy study of the precipitation of nanometric oxides in ODS ferritic steels obtained by the STARS route

Transmission electron microscopy and X-ray absorption spectroscopy study of the precipitation of nanometric oxides in ODS ferritic steels obtained by the STARS route

Nerea Ordás[a], Emma Gil[a], Arturs Cintins[b], Vanessa de Castro[c], Teresa Leguey[c], Iñigo Iturriza[a], Juris Purans[b], Andris Anspoks[b]

[a] Ceit-IK4, 20018 San Sebastian, Spain
[b] Institute of Solid State Physics, University of Latvia, 1063 Riga, Latvia
[c] University Carlos III Madrid, 28911 Leganés, Madrid

ABSTRACT (preliminary)

Oxide Dispersion Strengthened Ferritic Stainless Steels (ODS FS) are candidate materials for structural components in future fusion reactors. Their high strength and creep resistance at elevated temperatures and their good resistance to neutron radiation damage is obtained through extremely fine microstructures containing a high density of very stable nanometric precipitates, generally yttrium and titanium oxides.

This work shows transmission electron microscopy (TEM) and extended X-ray absorption fine structure (EXAFS) characterization of Fe-14Cr-2W-0.3Ti-0.24Y ODS FS obtained by the STARS route (Surface Treatment of gas Atomized powder followed by Reactive Synthesis), an alternative method to obtain ODS alloys that avoids the mechanical alloying to introduce Y_2O_3 powder particles. In this route, FS powders already containing Ti and Y, precursors of the nanometric oxides, are obtained by gas atomization. Then, a metastable Cr- and Fe- rich oxide layer is formed on the surface of the powder particles. During consolidation by HIP at elevated temperatures, and post-HIP heat treatments above the HIP temperature, this oxide layer at Prior Particle Boundaries (PPBs) dissociates, the oxygen diffuses, and Y-Ti-O nano-oxides precipitate in the ferritic matrix.

TEM characterization combined with XAFS and XANES analyses have proven to be practical tools to follow the evolution of the nature of the different oxides present in the material during the whole processing route and select appropriate HIP and post-HIP parameters to promote profuse and fine Y-Ti-O nanometric precipitates.

1. Introduction

Oxide dispersion strengthened ferritic stainless steels (ODS FS) are candidates for structural components in future fusion and fission reactors, concentrated solar power plants, chemical reactors or advanced coal fired plants, thanks to their high strength and creep resistance at elevated temperatures, as well as to their good resistance to neutron radiation damage [1], [2], [3], [4], [5], [6], [7], [8], [9], [10]. Their outstanding behaviour is a direct consequence of their very fine grain size, and the presence of very stable oxide nanoparticles with size smaller than 10 nm, generally yttrium and titanium complex oxides, with high temperature stability [11], [12], [13]. These oxides have a pinning effect on dislocations and are sinks for irradiation induced defects [14], [15].

The conventional processing route of ODS FS includes mechanical alloying (MA) of elemental or prealloyed powders with Y_2O_3 particles to dissolve the yttrium in the ferritic matrix, followed by consolidation by hot isostatic pressing (HIP) or hot extrusion to promote the nucleation of the nanometric oxides, and finishes with thermo-mechanical treatments (TMTs) to refine the grain size or to develop a stable dislocation sub-grain structure.

However, MA involves several drawbacks including its time and cost inefficiency, the contamination from the grinding media, jars or atmosphere, the difficulty in controlling the alloy homogeneity, which have limited the widespread use of commercial ODS alloys to niche applications.

Ceit-IK4 has developed a route to produce ODS FS with composition Fe-14Cr-2W-0.3Ti-0.3Y_2O_3 (in wt.%) called STARS (Surface Treatments of gas Atomized powder followed by Reactive Synthesis) [16], [17], [18] and based on the Gas Atomization Reaction Synthesis (GARS) method developed by Rieken et al. [19], [20]. This route avoids the traditionally used MA process and, hence, overcomes the typical problems of ODS alloys: the material is free from contamination from grinding media or atmosphere, the loss of ductility associated to MA disappears, the processing time of the powders is reduced from days to hours per batch, and the size of each powder batch can rise from several to hundreds of kilograms. .

The STARS route is fundamentally based on the internal oxidation process. Powders already containing Y are obtained by gas atomization, using an inert gas (argon) and, therefore, thei roxygen concentration is lower than the required to form the Y-Ti-O nanoparticles. The surface of the as-.atomized powders is oxidized and a metastable Cr- and Fe- rich oxide layer is formed on the surface of the powder particles [18]. During consolidation by HIP at elevated temperatures (that can reach 1300 °C), this oxide layer dissociates, its oxygen diffuses inside the grains and reacts with the titanium and yttrium dissolved in the ferritic matrix and forming yttrium-rich intermetallic compounds, respectively. As a result, Y-Ti-O nano-oxides precipitate. Post-HIP heat treatments (HT) performed above the HIP temperature dissolve most of the remaining oxides at PPBs. The temperature of these HT must be carefully chosen to avoid detrimental effects in the final microstructure, like grain growth, the development of Thermally Induced Porosity (TIP) or coalescence of residual carbonitrides, Ti(C,N). Finally, TMTs are performed to promote grain refinement and a suitable crystallographic texture.

Understanding of mechanisms involved in the development of these oxide nanoparticles and their role in the performance of ODS steels requires the use of advanced structural characterization tools with near atomic resolution, such as transmission electron microscopy (TEM), atom probe tomography (APT) and small angle neutron scattering. Advanced TEM and APT provide of vital information regarding the spatial distribution, chemistry and crystal structure of nanoparticles. However, they can only study small sample volumes, and moreover, there are strict requirements for sample preparation. In contrast, X-ray Absorption Fine Spectroscopy (XAFS) provides a practical way to study minority elements, giving unique and direct information on the chemical and physical state of dilute ODS species [21], [21], [22], [23].

In this work, XAFS is used to study the evolution of Y-Ti-O nanometric particles during the fabrication of ODS FS following the STARS route. The results, compared to XPS (X-ray photoelectron spectroscopy), SEM and TEM characterization, provide new insights on the atomic scale mechanisms of the ODS particle formation, nucleation and growth, and are useful tool to evaluate the effectiveness of HIP and post-HIP HT in developing a profuse nanometric oxide precipitation.

2. Experimental procedure

Powders with the target composition Fe-14Cr-2W-0.3Ti-0.24Y (wt. %) were produced by close-coupled gas atomization at Ceit-IK4. The particle size of the powders used in this work is in the range 20-45 μm. The chemical composition of the as-atomized powder was analysed by inductively coupled plasma optical emission spectroscopy (ICP-OES). Nitrogen and oxygen concentrations were obtained with the inert gas fusion principle, and carbon and sulphur with the combustion infrared detection technique. The obtained values are shown in Table 1.

Table 1. Composition of as-atomized powder (wt.%).

Element	Fe	Cr	W	Ti	Y	Al	O	N	C	S
	83.33	14.08	2.00	0.32	0.34	0.08	0.025	0.001	0.009	0.002

Atomized powders were heat treated to adjust oxygen content to allow complete oxidation of the yttrium present. Powders were consolidated by HIP (Hot Isostatic Pressing), at three different conditions: 900 °C, 1220 °C and 1300 °C, applying 140 MPa during 2 hours, to study the microstructure evolution of these ODS FS during dispersoid formation. HIPped samples at 900 °C and 1220 °C were subjected to heat treatments (HT) in argon atmosphere during 2 hours, at 1220 °C and 1300 °C, and at 1270 °C and

1320 °C, respectively, to study the stability of the microstructures obtained after HIP. Table 2 shows the samples analized in this work.

Table 2. ODS ferritic steel samples studied by XAS.

Code	Description
N1	As atomized powder
N2	Surface treated powder
N3	Sample HIPped at 900 ºC, 140 MPa, 2 h
N4	Sample HIPped at 900 ºC, 140 MPa, 2 h + HT at 1220ºC, 2h
N5	Sample HIPped at 900 ºC, 140 MPa, 2 h + HT at 1300ºC, 2h
N6	Sample HIPped at 1220 ºC, 140 MPa, 2 h
N7	Sample HIPped at 1220 ºC, 140 MPa, 2 h + HT at 1270ºC, 2h
N8	Sample HIPped at 1220ºC, 140 MPa, 2 h + HT at 1320ºC, 2h
N9	Sample HIPped at 1300 ºC, 140 MPa, 2 h

The microstructure of the powders and specimens after HIPping and HTs was observed by FEG-SEM (Field Emission Gun-Scanning Electron Microscope) equipped with an EDS (Energy Dispersive Spectrometry) analyser. The consolidated samples were also analysed by transmission electron microscopy (TEM) with focus on the nanoparticle dispersion. A JEOL 3000F FEG-TEM microscope operated at 300 keV and equipped with an EDS analyser and an Enfina detector for EELS (Electron energy loss spectroscopy) analysis was used for this characterization. The nanoparticle number densities were estimated in at least five different volumes of the order of 10^{-20} m^3, and the thickness of the foils was determined with the log-ratio technique, where the inelastic mean free path was calculated from the formula derived by Malis et al.[23].

3 mm diameter disks for TEM characterization were prepared by electropolishing in a TENUPOL-5 twin-jet polisher using 5% $HClO_4$ + 95% CH_3OH as electrolyte. Before each TEM session, the samples were additionally cleaned for 5 minutes in a plasma cleaner.

X-ray absorption spectroscopy measurements were performed at the bending-magnet SAMBA beamline at the SOLEIL synchrotron radiation facility [24]. The storage ring operated in the multibunch hybrid mode at the energy E=2.75 GeV and the maximum stored current I_{max}=430 mA. The steel samples were measured in fluorescence mode, whereas reference samples were measured in transmission mode. The x-ray beam was monochromatized by sagittal focusing double-crystal Si(220) monochromator, two ionization chambers filled with nitrogen gas were used to detect incoming and transmitted intensities, Camberra 36-elements monolithic planar Ge pixel array detector was used to measure fluorescence signal. All measurements were performed at room temperature in ambient conditions. Titanium and yttrium foils as well as three powders (polycrystalline Y_2O_3 and TiO_2, nanocrystalline Y_2O_3 (6 nm), and crystalline Y_2Fe_{17}) were used as reference samples.

X-ray absorption spectra in near-edge (XANES) and post-edge (EXAFS) regions at the Ti, Fe and Y K-edges were analysed using conventional methodology [25] and two software packages - EDA [26] and Athena [27]. Theoretical calculations of X-ray absorption spectra were performed using the FEFF8.5L [28] codes.

3. Results

3.1. Microstructure of atomized powders

The as-atomized powders are mainly spherical, although some of them contain satellites and splat caps (Figure 1a) caused by collisions between particles during solidification. The internal microstructure of powders is fully ferritic, with a wide grain size distribution (Figure 1b).

Yttrium has a very limited solubility in iron and steel, even at high temperature (about 0.12 wt.% at 1320 °C [29], [30], and 0.018 wt.% at 800 °C [31]) and negligible at room temperature. Consequently, once

the atomized melt droplets solidify, yttrium is rejected to highly disordered areas during nucleation and growth of the ferritic grains, resulting in yttrium segregation and precipitation at triple points and, in a lesser extent, grain boundaries. It was found that the length scale of these yttrium-rich precipitates is correlated with the powder particle size and, therefore, is controlled by the solidification rate. Yttrium remains in oversaturated solid solution in powder particles below 5 µm in diameter and, hence, do not contain Y-rich segregates (Figure 2a and b). Particles with size ranging from 5 to 20 µm contain nanometric discrete yttrium-rich precipitation (Figure 2c). Powder particles with diameter between 20 and 45 µm contain a discrete distribution of an intergranular Y-rich phase at the surface and in the interior, whose size increases with powder particle size (Figure 2d to f, black arrows). Finally, this Y-rich phase evolves towards micrometric scale in the largest particles, with high contiguity in powders above 63 µm (Figure 2e, f, h and i, black arrows). Some of these yttrium-rich particles seem to have nucleated from nanometric precipitates (white arrows in Figure 2 e, f, h and i). EDS analysis suggests that the yttrium-rich phase, which also contains iron, nucleates from Y-rich oxides, probably Y_2O_3. Compared to larger powder particles (Figure 2g), yttrium-rich precipitation at the surface of particles between 20 and 45 µm is limited to grain boundaries (Figure 3a). The presence of metastable chromium-rich oxide particles at the surface of as-atomized powders (Figure 3b), observed by EDS analysis, was confirmed by XPS (X-ray photoelectron spectroscopy) in a previous work [18].
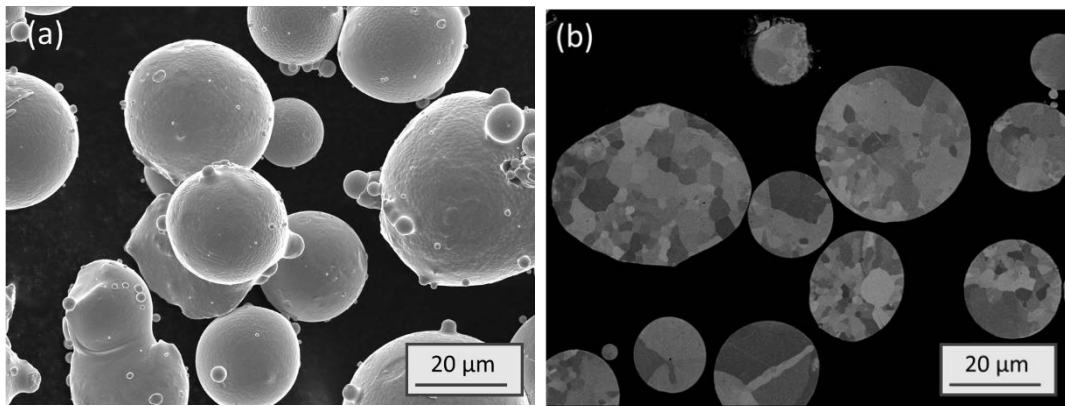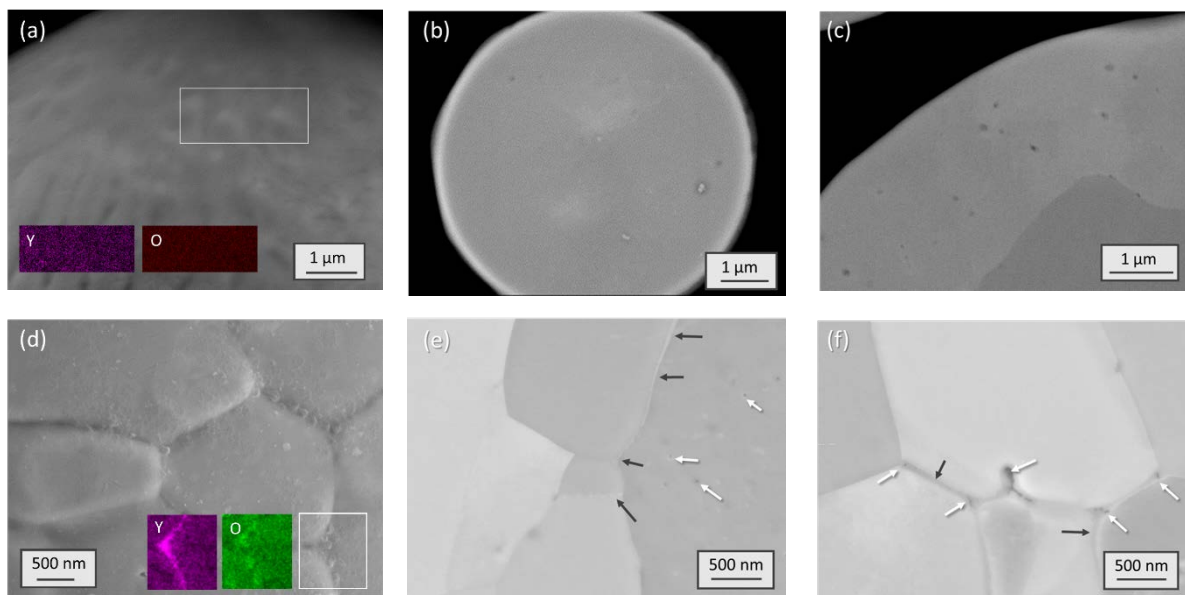

Figure 1. SEM images of a) surface of as atomized powder, N1 (SE), and b) internal microstructure (BSE).
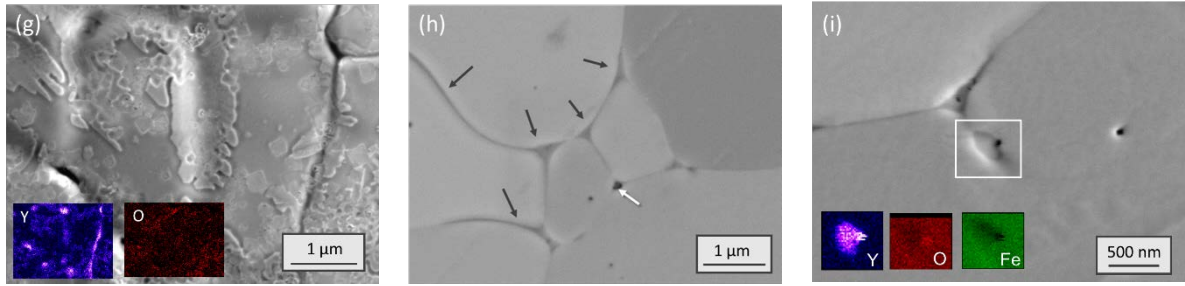

4

Figure 2. SEM images of as-atomized powder (N1) with particle size below 20 µm, (a) to (c), between 25 and 45 µm, (d) to (f) and between 63 and 75 µm, (g) to (i). (a), (d) and (g) correspond to surface of powder particles, whereas (b), (c), (e), (f), (h) and (i) show internal microstructure.
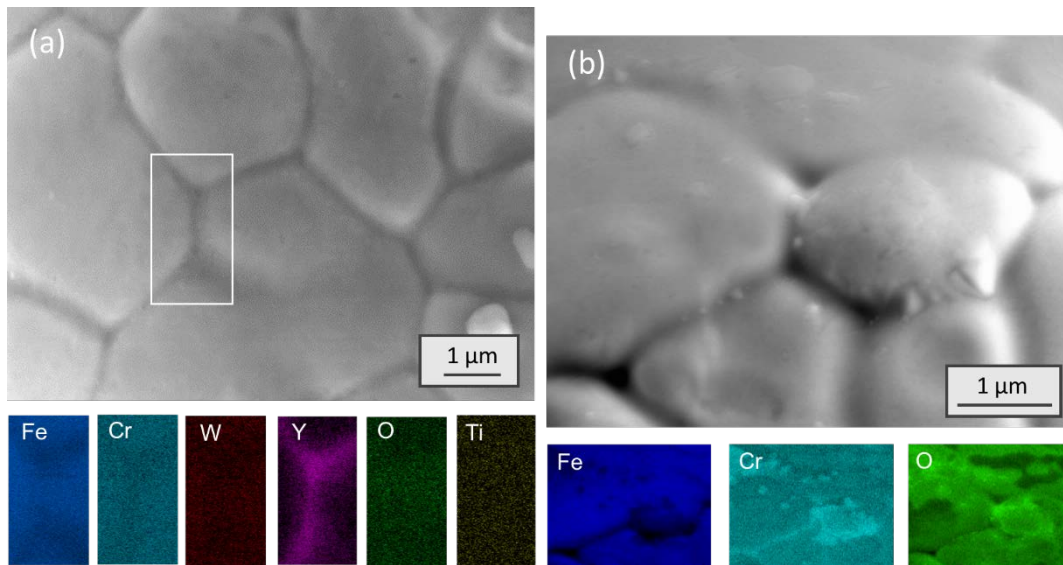

Figure 3. SEM images and EDS mappings of surface of as-atomized powders (20-45 µm) showing (a) Y-rich precipitation at grain boundaries and (b) Cr-rich oxides.

The heat treatment of the powder under oxidizing atmosphere resulted in an increase in the roughness of the surface of powder particles and the development of continuous chains preferentially located at grain and sub-grain boundaries (Figure 3). EDS (Figure 4) and XPS analyses confirmed the development of a ~19 nm thick oxide layer, consisting of a continuous Fe_2O_3 layer, and submicrometric yttrium and Y_2O_3 particles at grain and sub-grain boundaries, flanked by Cr_2O_3 chains[18]. Also titanium enrichment was detected in the chains developed. However, the internal microstructure (not shown here) remained the same as in as-atomized powders, and the yttrium-rich phase remained apparently free from oxidation.
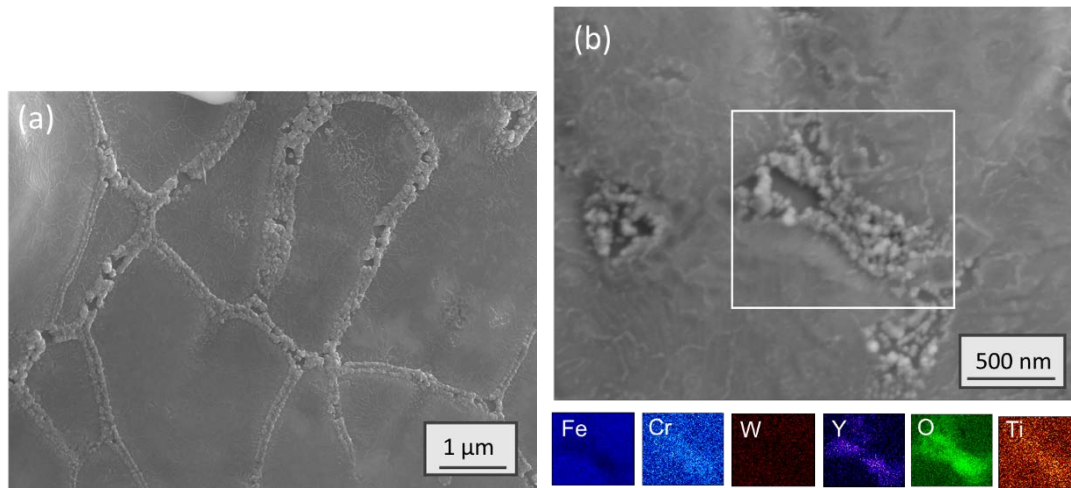
Figure 4. SEM images and EDS mappings of surface of powders heat-treated under oxidizing atmosphere (N2).

3.2. Microstructure after HIP

3.2.1. Low temperature consolidation

The sample consolidated at the lowest temperature, 900 °C, during 2 hours (N3) did not reach full density, and residual porosity was found at some triple points (Figure 5a). A continuous layer, identified by EDS as Ti- and Y-rich particles (probably oxides), was found along prior particle boundaries (PPBs) (Figure 5b). The presence of Al at PPBs is associated to contamination. The Cr_2O_3 metastable oxide initially present at PPBS together with Fe_2O_3 [17] was hardly resolved by EDS. Additionally, this sample contained an internal structure of (Y, W)-rich particles (light grey submicrometric precipitates in Figure 5a and b), that resembles that of previous as-solidified intergranular Y-rich precipitates (Figure 2e and f). From these observations it can be derived that these consolidation parameters are insufficient to activate the oxygen diffusion between the partially dissociated oxides at PPBs and the (Y, W)-rich particles. The analogy between this microstructure and that observed by Rieken after consolidation of Fe-16Cr-0.31Y-0.12Y (at.%) at 700 °C and 200 MPa during 4 hours [19], [20] leads to assume that these particles are Fe-(Y,W) intermetallics.

Heat treatments at high temperature (1220 and 1300 °C, N4 and N5, respectively) were performed after HIP at low temperature, to promote the oxygen exchange between the metastable oxides that remained at PPBs and the (Y, W)-rich particles inside grains. As it is displayed in Figure 5c, the oxides present at PPBs seemed to be almost fully dissolved, and (Y, W)-rich particles could not be observed inside grain boundaries. However, with post-HIP heat treatments, ferritic grains grown (especially the largest grains, see *Table 3*), some Ti- and Y-rich submicrometric particles (probably Y_2O_3 and Ti(C,N)) remained at PPBs (Figure 5d-f), and the size and number of Ti-rich particles increased with post-HIP heat treatment. A very fine distribution of Y-rich nanoparticles could be also observed, mainly close to PPBs and grain boundaries (Figure 5d and e). These microstructural changes are clear evidence of the oxygen exchange between the mestastable oxides at PPBs and the (Y, W)-rich precipitates, to form a nanometric dispersion of oxides. These heat treatments performed without external pressure caused reopening of internal pores inside powder particles, collapsed during HIPping. As a result, thermally induced porosity (TIP) developed (Figure 5c, white arrow). The fact that these samples underwent grain growth, in some cases up to dimensions close to the initial powder particle size, suggests that the precipitation of the nanometric Y-rich particles took place at the maximum temperature, probably not at the early instants of the maintenance. Otherwise, they would have been able to hinder grain growth.
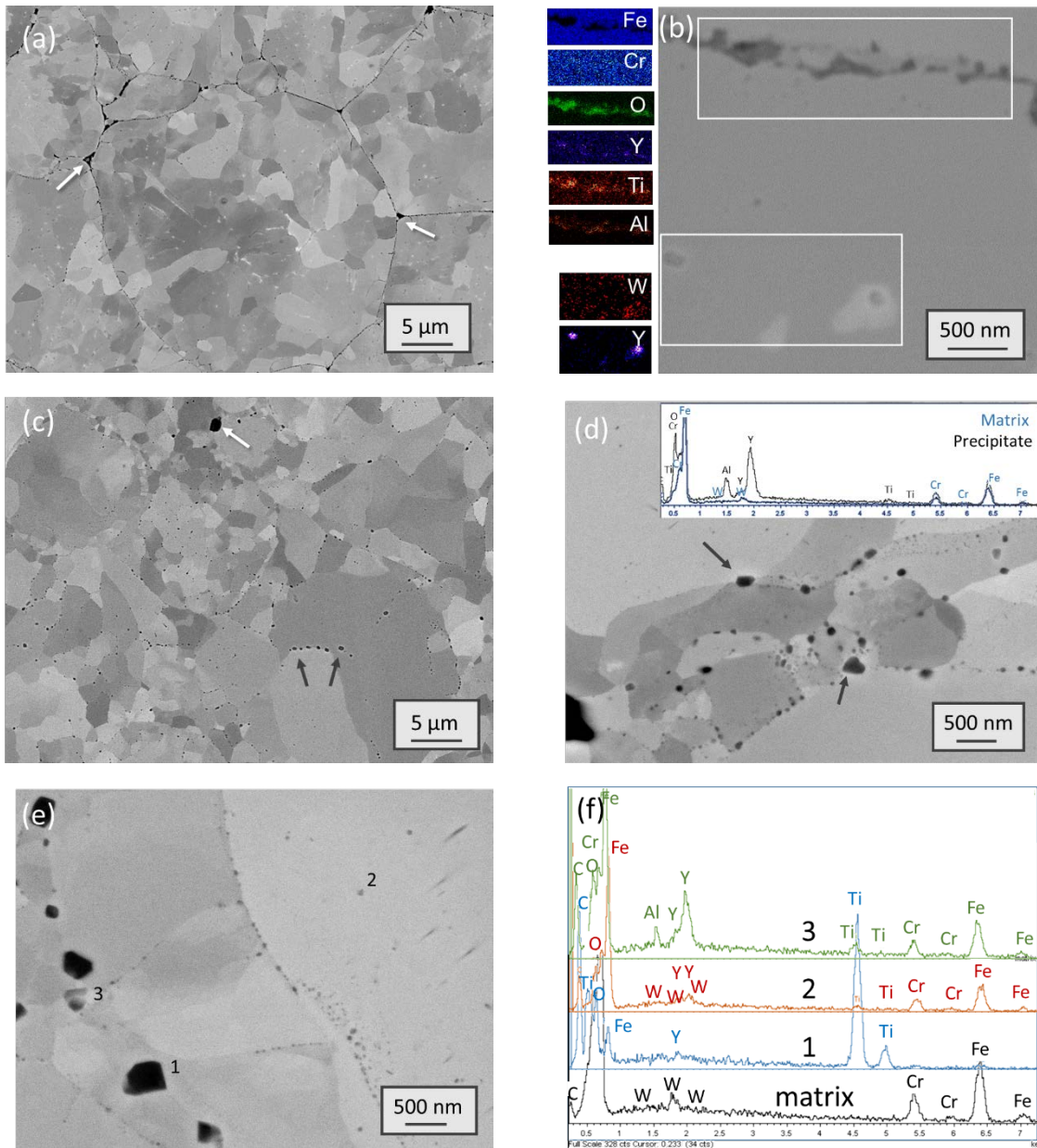
Figure 5. SEM Microstructures after low temperature (900 °C) HIP, N3 (a and b), and after post HIP heat treatment at 1220 °C (c and d), N4, and 1300 °C (e and f), N5.

Table 3. Grain size distribution after HIP at 900 °C and after post-HIP heat treatments.

Code	Description	Grain size distribution by volume (µm)		
		D10	D50	D90
N3	HIP 900 °C	2,5	7	15
N4	HIP 900 °C + HT 1220 °C	3,5	9,5	22
N5	HIP 900 °C + HT 1300 °C	3,5	10	23,5
N6	HIP 1220 °C	3	10	20
N7	HIP 1220 °C + HT 1270 °C	3,25	10	19,5
N8	HIP 1220 °C + HT 1300 °C	2,5	10	20,5
N9	HIP 1300 °C	3	10	22,5

3.2.2. Consolidation at high temperature and post HIP heat treatment

Fully dense samples, were obtained after consolidation at high temperature (1220 and 1300 ºC, N6 and N9, respectively). Values of grain size distribution from *Table 3* and SEM observation of samples HIPped at 1220 °C and 1300 °C, depicted in Figure 6 a and c, confirmed that an increase in 80 °C did not lead to noticeable microstructural changes. Metastable oxides at PPBs were completely dissociated after HIP, and only discrete submicrometric precipitates remained, with sizes ranging from 100 to 500 nm. EDS analysis suggests they are mainly rich in Ti (probably Ti(C,N) or Ti_xO_y), although minor presence of Y-rich precipitates (probably Y_2O_3) was also detected. An extremely fine precipitation of Y-rich nanoparticles of about 20-30 nm could be observed at high magnifications, preferentially at the vicinity of PPBs and grain boundaries (Figure 6b and d), evidencing again an oxygen exchange reaction between the PPBS and the interior of grains to form more thermodynamically stable oxides.
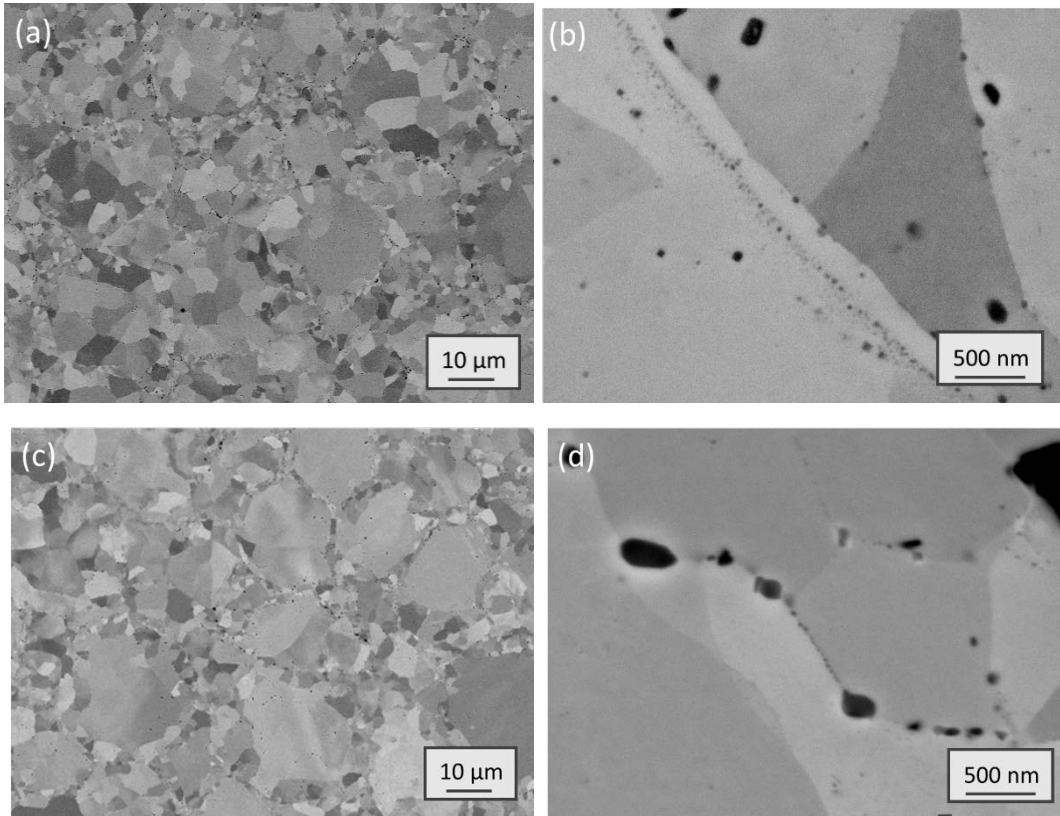

Figure 6. SEM Microstructures after HIPing at 1220 °C (a, b), N6, and 1300 °C (c, d), N9.

TEM was used to study in more detail the nanoparticles dispersion. Figure 7 shows bright field (BF) images of nanoparticles for samples N6 and N9, consolidated at 1220 °C (Figure 7 (a, b)) and 1300 ºC (Figure 7 (c, d)), confirming the spatial distribution previously observed by SEM. Larger nanoparticles, with round or rod-like morphologies, are mainly located at or near grain boundaries, while smaller nanoparticles having round or square-faceted morphologies are distributed inside grains, although the nanoparticle density decreases with increasing distance to the grain boundaries. Figure 8 depicts cumulative histograms showing the size distribution of the nanoparticles present after both HIP treatments, N6 and N9. The distributions are similar but, as evidenced in the cumulative histograms, there are more small nanoparticles in the batch consolidated at 1220 °C. In particular, 89% of the measured nanoparticles are < 50 nm (and 28% < 10 nm) in the sample consolidated at 1220 °C, being the average size of small nanoparticles 16 ± 10 nm. 70% of the measured nanoparticles are < 50 nm (and 40% < 10 nm) in the sample consolidated at 1300 °C, being the average size of small nanoparticles 15 ± 11 nm.
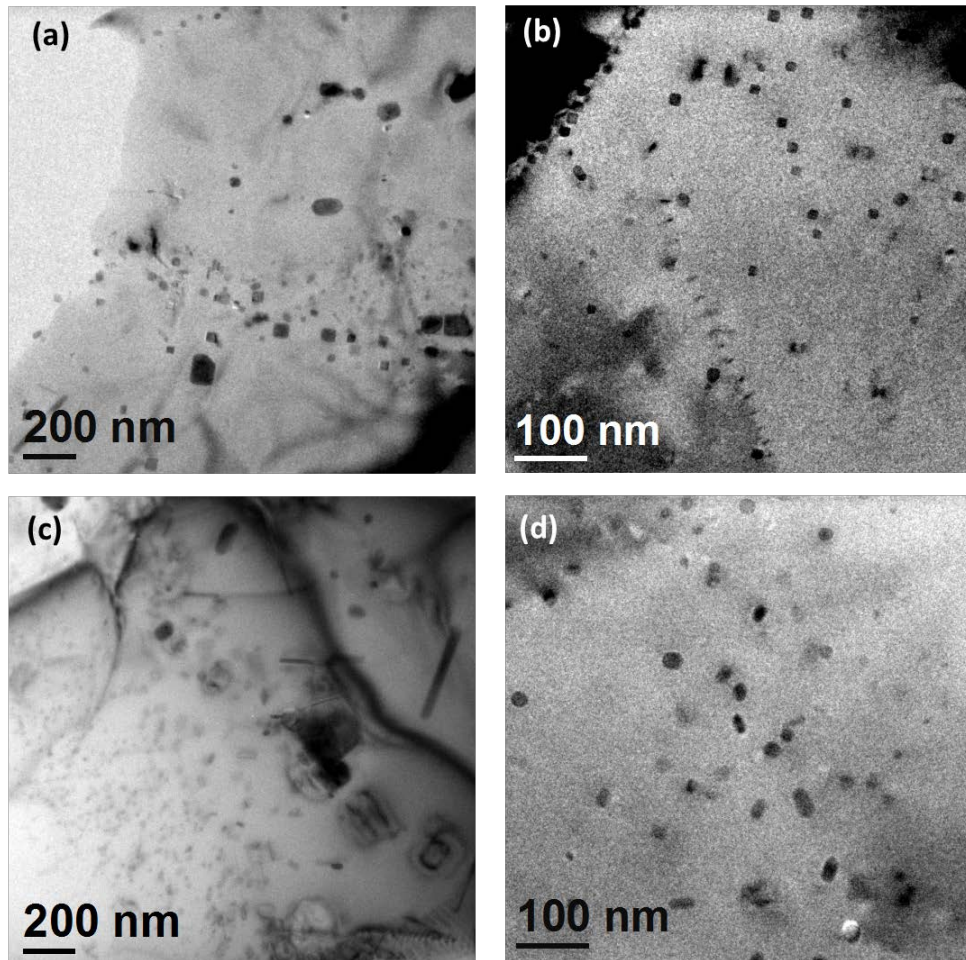
Figure 7. BF images of the samples consolidated at (a, b) 1220 °C, N6, and (c, d) 1300 °C, N9.
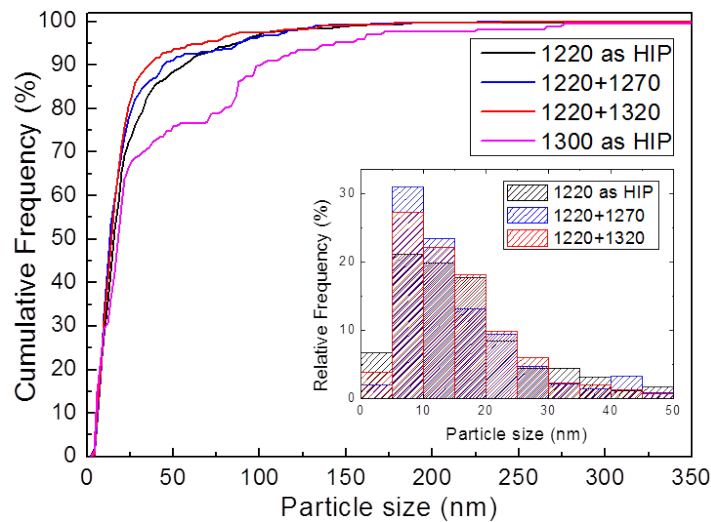

Figure 8. Cumulative histograms of the nanoparticle size distribution for the samples consolidated at 1220 °C (N6) and 1300 °C (N9) and for the samples heat treated at 1270 °C and 1300 °C after HIP at 1220 °C (N7 and N8, respectively). The inset shows the distribution of nanoparticles <50 nm for the three samples consolidated at 1220 °C (as-HIP, heat treated at 1270 °C and heat treated at 1320 °C).

Density measurements were done on sample N6, consolidated at 1220 ºC. Number densities of visible nanopartices varied between $(2.1 ± 0.4) \times 10^{21}$ m^{-3} and $(8 ± 2) \times 10^{21}$ m^{-3}. These densities are one order of magnitude lower than the ones found by TEM in other ODS steels having similar compositions [32],

[33]. The chemical composition and crystal structure of the small nanoparticles was studied by EDS and high resolution electron microscopy (HREM). Figure 9 shows examples of nanoparticles for samples N6 and N9, consolidated at 1220 °C and 1300 °C, respectively. In both cases, all the measured particles were Y and Ti-rich, and ~ 80% also contained Al as contamination. Si was also detected in some of them. Nanoparticles are identified by HREM as either Y_2TiO_5 or $Y_4Al_2O_9$ ternary oxides.
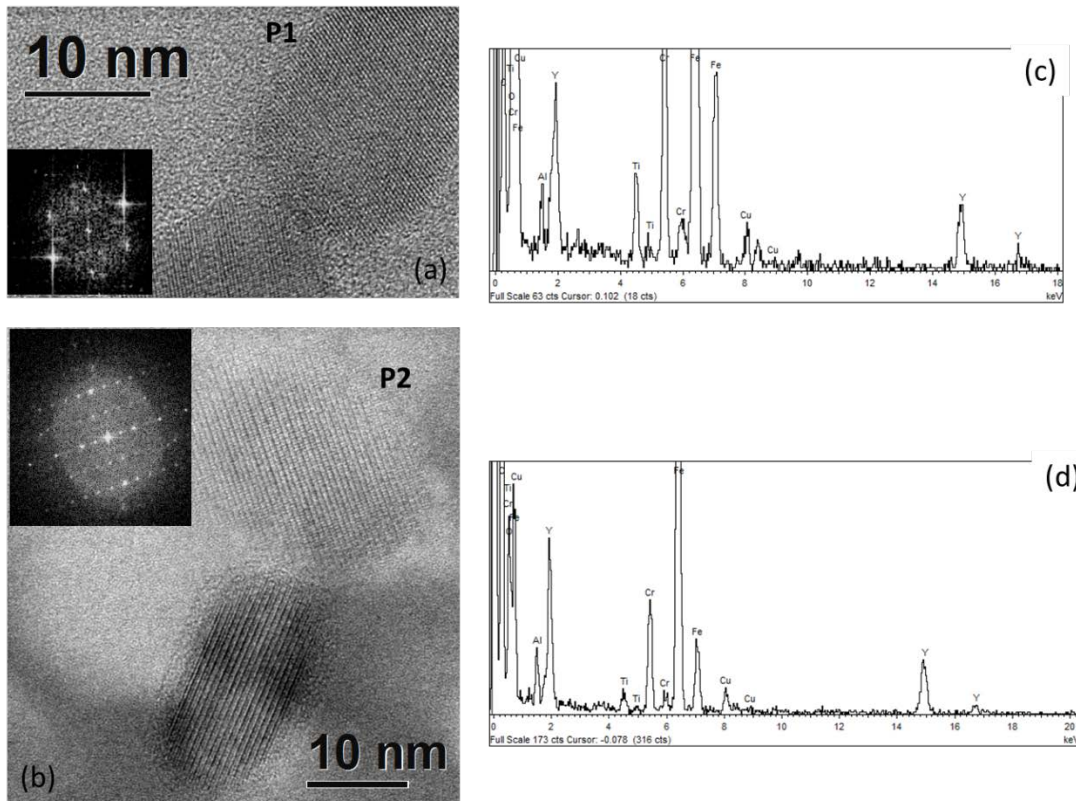

Figure 9. (a) HREM image of nanoparticle P1 present in the sample consolidated at 1220 °C (N6) and corresponding FFT and (b) EDS spectrum of the nanoparticle, identified as Y_2TiO_5 in zone axis [123]. (c) HREM image of nanoparticle P2 present in the sample consolidated at 1300 °C (N9) and corresponding FFT and (d) EDS spectrum of the nanoparticle, identified as $Y_4Al_2O_9$ in zone axis [110].

Post-HIP heat treatments of samples HIPped at 1220 °C above the HIP temperature did not cause grain growth (*Table 3*) demonstrating that the nanoparticles precipitated during HIPping were effective in controlling grain growth. However, TIP developed (Figure 10a), and submicrometric particles at grain boundaries coarsened (compare with Figure 6a and c). EDS analysis showed that most of them are Ti-rich particles, probably Ti(C,N) and, in some cases, a W-rich core (probably an oxide) was observed (Figure 10c and d).
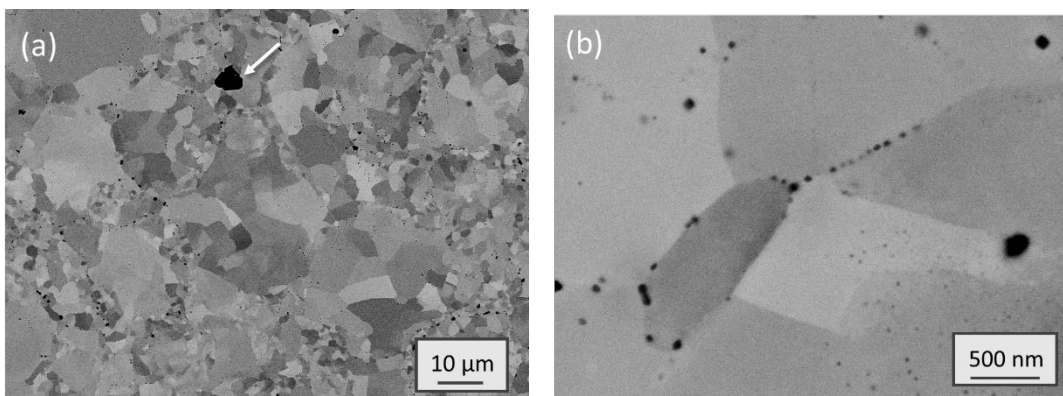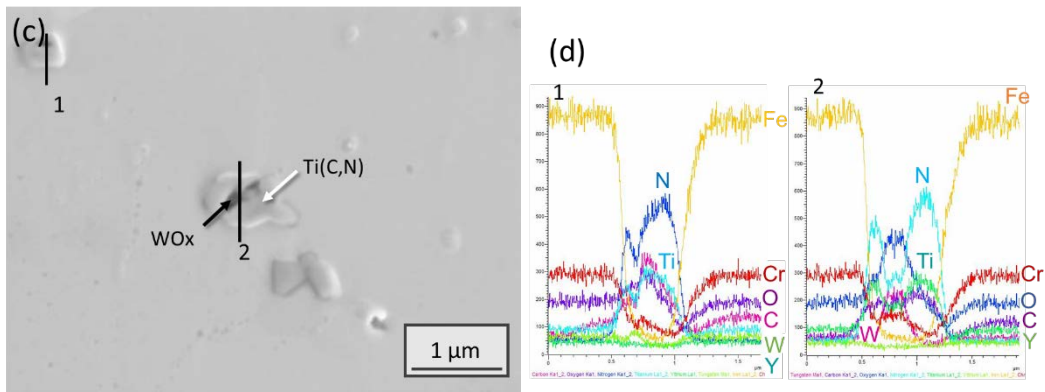
Figure 10. SEM Microstructures of sample N8, HIPped at 1220 °C and heat-treated at 1320 °C.

TEM images of the nanoparticle dispersion after the heat treatments are depicted in Figure 11. Their spatial distribution is similar to that of as-HIPped samples. Very few rod-like and square-faceted particles are detected after the heat treatments, being most of them round-like. Figure 8 presents cumulative histograms showing their overall size distribution. The histograms comparing the distribution of the smaller nanoparticles before and after the heat treatments are also depicted as an inset. Alike in the as-HIPped samples, after heat treating at 1270ºC and 1320 °C, 91% and 93% of particles, respectively, are smaller (< 50 nm) Y, (Al, Ti) oxides. After both heat treatments, 33% of nanoparticles are below 10 nm. In both cases, their mean diameter is 15 ± 9 nm, very similar to that of the as HIP samples (17 ± 11 nm). The slight growth of nanoparticles < 5 nm observed after both post-HIP heat treatments could be an artefact due to sample heterogeneities.
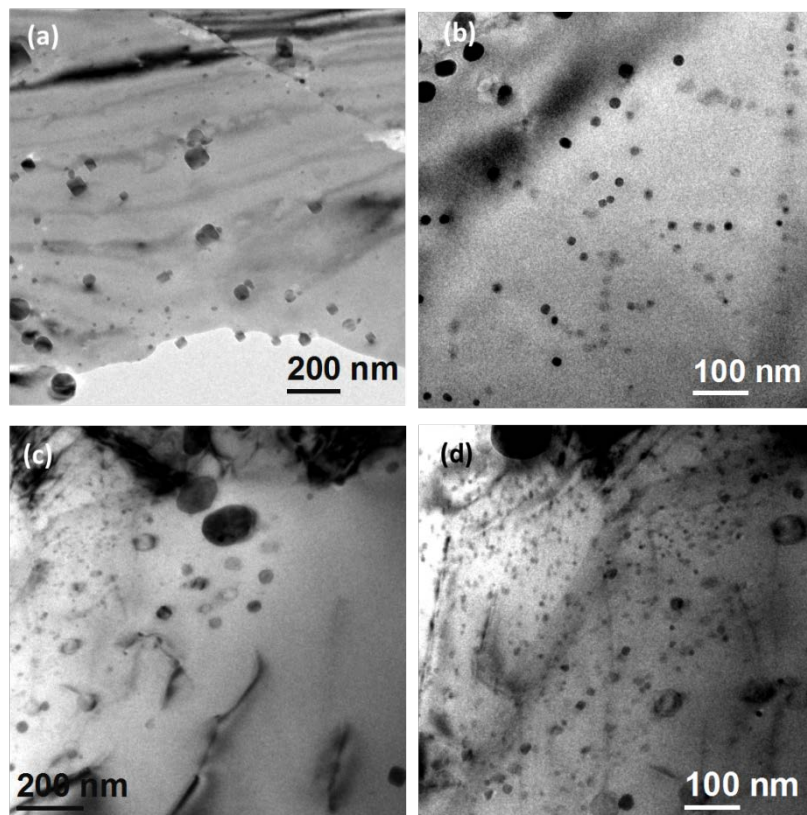

Figure 11. BF images of samples consolidated at 1220 °C and heat treated at (a, b) 1270 °C (N7) and (c, d) 1320 °C (N8).

11

After the heat treatment at 1270 ºC, the number densities of visible nanopartices ranged between (0.70 ± 0.14) x 10^{21} m^{-3} and (6.9 ± 1.4) x 10^{21} m^{-3}. After the heat treatment at 1320 °C densities ranged between (0.45 ± 0.09) x 10^{21} m^{-3} and (5 ± 1) x 10^{21} m^{-3}. In both cases, densities were of ~ 5 x 10^{21} m^{-3} in most regions. These densities are similar to the ones found in the as HIP samples.

HREM measurements and EDS spectra from the corresponding nanoparticles are shown in Figure 12. As in the case of the as-HIPped alloy, most particles are identified as Y_2TiO_5 or $Y_4Al_2O_9$ ternary oxides.
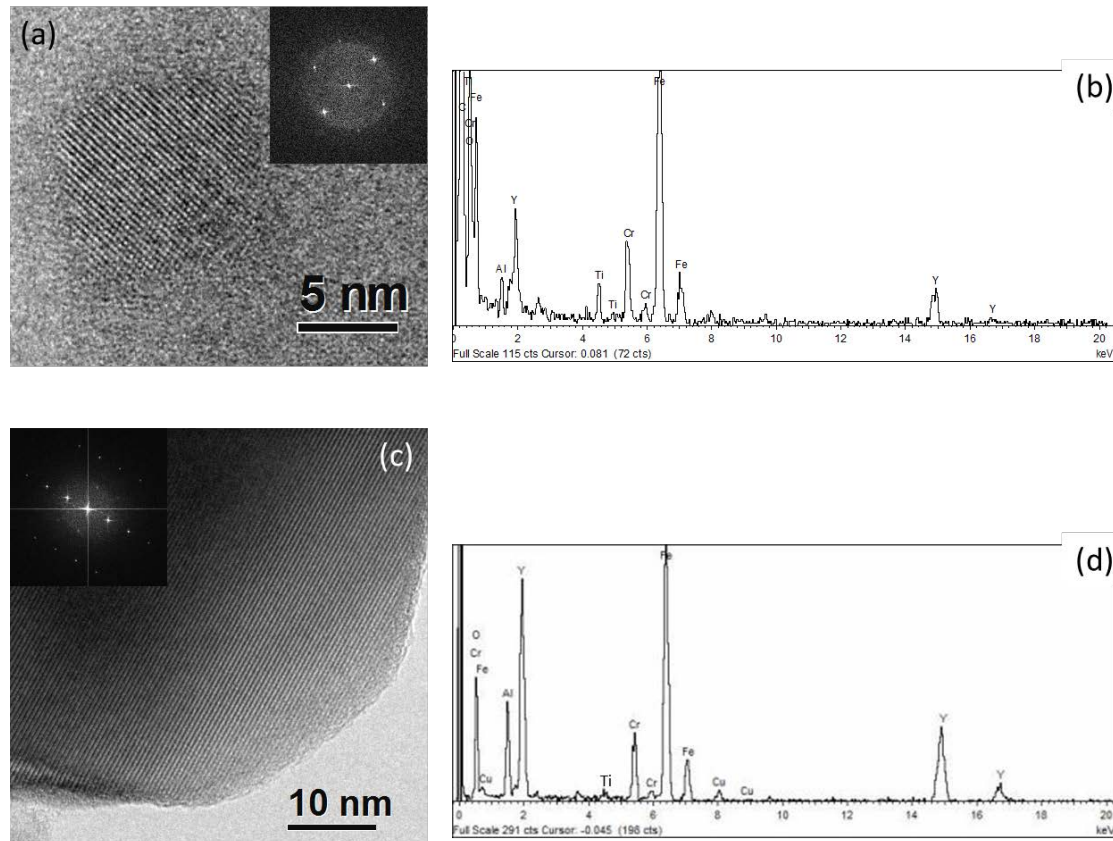

Figure 12. (a) HREM image of a nanoparticle from sample consolidated at 1220 °C and heat treated at 1270 °C (N7) and corresponding FFT and (b) EDS spectrum of the nanoparticle, identified as Y_2TiO_5 in zone axis [262]. (c) HREM image of a nanoparticle from sample consolidated at 1220 °C and heat treated at 1320 °C (N8) and corresponding FFT and (d) EDS spectrum of the nanoparticle, identified as $Y_4Al_2O_9$ in zone axis [72-4].

1. XAS

The Y and Ti K-edge x-ray absorption spectra were obtained from the samples shown in Table 2. The good quality of the Y K-edge x-ray absorption spectra measured in fluorescence mode allowed performing the EXAFS spectra analysis up to k=10.5 Å^{-1} (Figure 13a). Two peaks at about 1.7 and 3.3 Å in the Fourier transforms (FT) of EXAFS are well resolved, besides smaller contributions from outer shells at higher distances (4-6 Å) (Figure 13b). The Ti K-edge x-ray absorption spectra are more noisy, because the photons with the corresponding energies 4900-5900 eV are absorbed in higher extent by the steel matrix, weakening the signal. Good quality EXAFS spectra could be obtained and analysed up to about 11 Å^{-1} (Figure 14a), with well resolved two peaks at about 2.2 and 4.5 Å in FTs followed by some outer shell contributions at least up to 7 Å (Figure 14b).
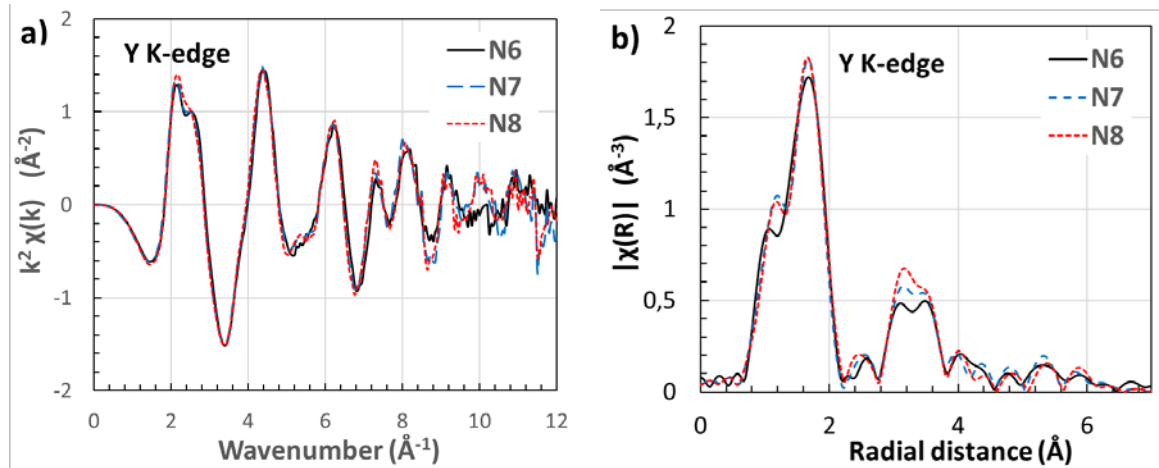
Figure 13. (a)Y K-edge EXAFS spectra of samples N6, N7 and N8 (HIPped at 1220 °C and heat treated at 1270 and 1320 °C), and (b) their Fourier transforms (FTs). Only FT moduli are shown.
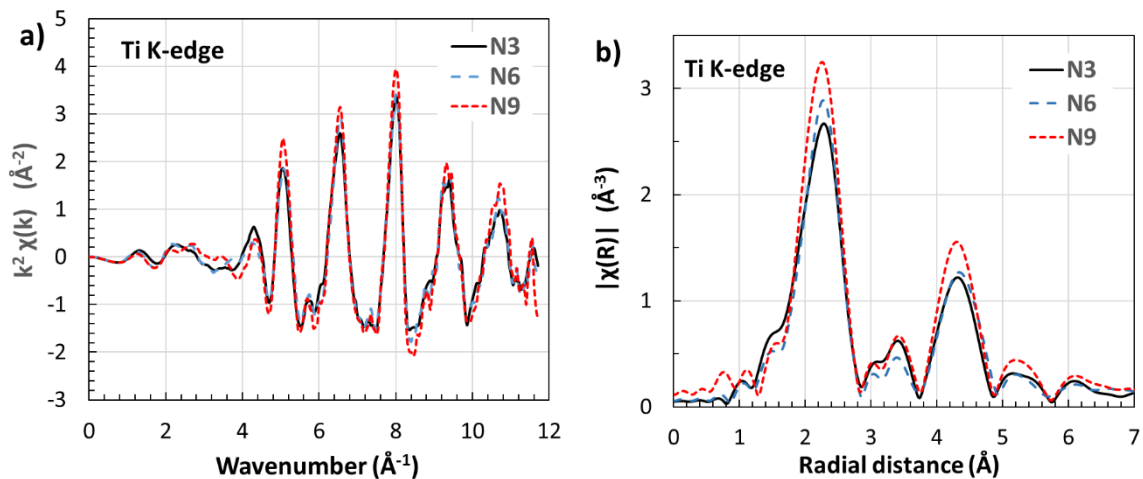

Figure 14. The Ti K-edge EXAFS spectra of samples N3, N6 and N9 (HIPped at 900 °C, 1220 °C and 1300 °C, respectively) (a), and their Fourier transforms (FTs) (b). Only FT moduli are shown.

1.1. Y K-edge spectra

The Y K-edge XANES spectra and Fourier transforms (FTs) of EXAFS spectra for ODS steel samples and two reference compounds (nanocrystalline Y_2O_3 (6 nm) and Y_2Fe_{17} intermetallic) are compared in Figure 15.

As can be seen, both XANES and FTs of the as-atomized powder (N1 in Figure 15a and b) are close to that of Y_2Fe_{17} intermetallic and differ from that of metallic Y foil. The as-atomized powder and Y_2Fe_{17} intermetallic have the similar position of the X-ray absorption edge (Figure 15a), and the position of peaks in FTs are also close to 4.5 Å (Figure 15b). This finding evidences that the majority of Y atoms in N1 sample is in metallic state (not oxidized), probably creating some intermetallic compounds (like Y_xFe_y), as suggested by EDS and SEM microstructural analysis of atomized powder (Figure 2i, for example). Nevertheless, the peaks in the range of 0.5-2 Å in FT for the as-atomized powder can be a sign of Y-O signal, confirming the presence of oxidized yttrium. This oxidized yttrium might correspond to the Y_2O_3 phase detected by XPS at the very surface of powder particles (up to 18 nm) [17] and by EDS (Figure 2d and g).

Yttrium in sample N3 HIPped at low temperature (900 °C) is present in an intermediate state, most probably containing a mixture of metallic and oxidized Y (Figure 15c and d). Subsequent post-HIP heat treatments (samples N4 and N5) performed at 1220 and 1300 °C lead to complete oxidation of yttrium

13

atoms. The XANES spectra of both samples mimic that of nanometric Y_2O_3: the peak at about 2.6 Å, which is characteristic of metallic yttrium, disappears completely in FTs, whereas the peak at about 1.7 Å due to the Y-O bonds increases significantly. These results are in line with SEM observations (Figure 5), and confirm that, after HIPping at low temperature, yttrium is not completely oxidized.

Consolidation at high temperatures (1220 and 1300 °C) leads to Y K-edge XANES spectra nearly identical to nano-Y_2O_3, indicating that the local symmetry (YO_6 octahedra) and the valence state (Y^{3+}) of yttrium atoms are similar (Figure 15e). FTs of EXAFS spectra in Figure 15d also support these conclusions, showing that characteristic Y-Me peak at 2.5 Å, corresponding to the distance to closest yttrium neighbours in Me matrix or in Y_xMe_y, disappears, and the feature at around 1.7 Å due to Y-O bonds appears. At the same time, some peaks, which are not present in FT of EXAFS for nano-Y_2O_3, can be noticed around 3.5 Å and starting from 4 Å. These peaks can be arguably attributed to a contribution of some complex Y-Me-O oxides, where Me can be any metal including Ti, Al, Cr. Heat treatments at high temperature (1270 and 1320 °C) after HIP at 1220 ºC do not have associated important changes in XANES and FTs of yttrium. They enhance the features of the spectra, for example, the amplitude of the FT peaks increases. This indicates that the local disorder around yttrium atoms decreases that can be a result of rearrangement of the oxide nanoparticles structure.
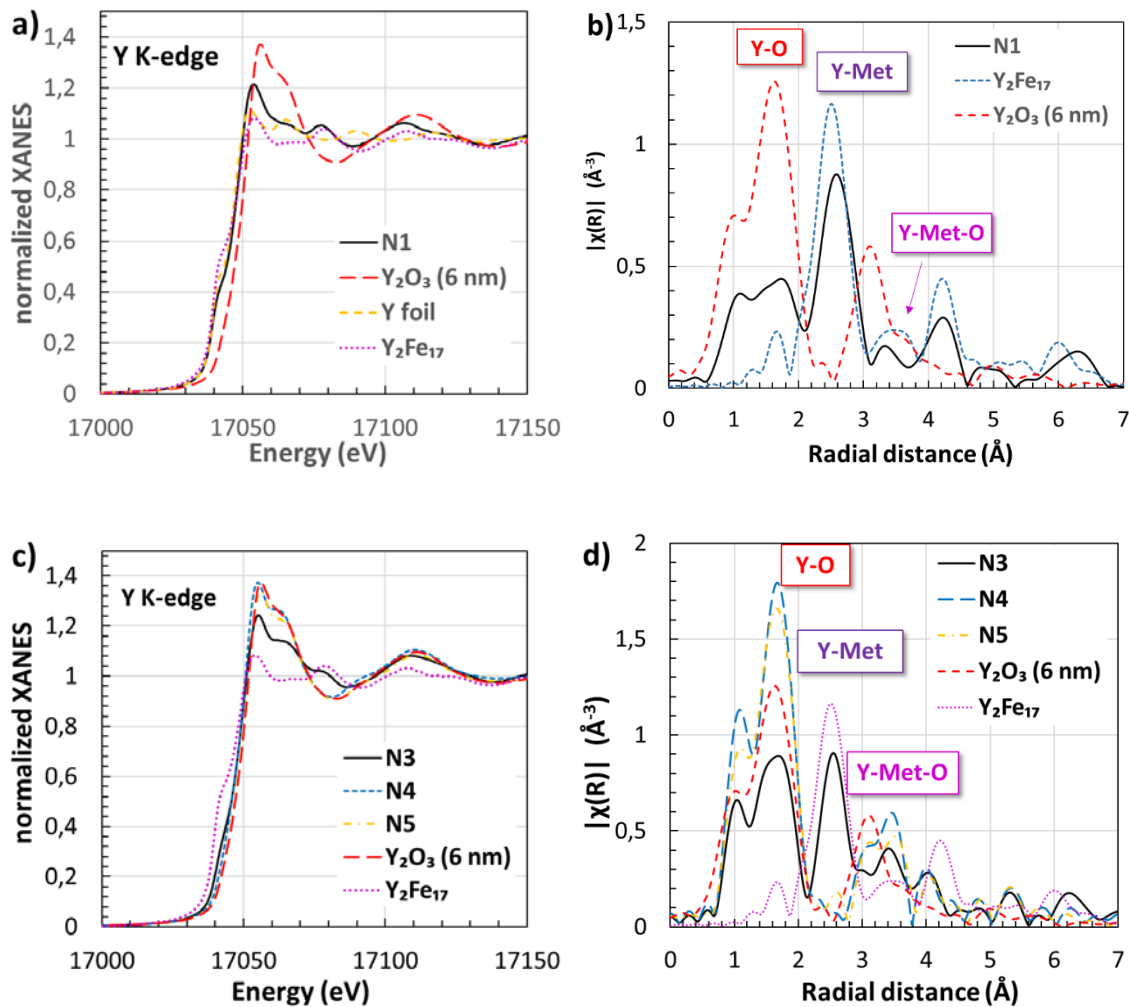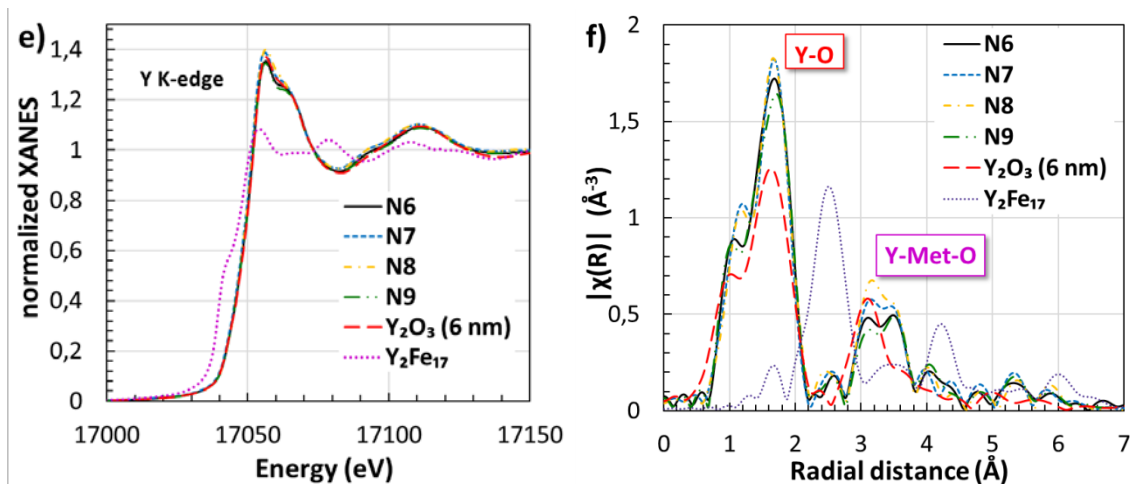
Figure 15. Y K-edge XANES (a, c and e) and Fourier transforms (FTs) of EXAFS (b, d and f) for analyzed samples and references (Y foil, Y_2O_3 and Y_2Fe_{17}). a) and b), N1 (as-atomized powder); c) and d), N3, N4 and N5 (HIPped at 900 °C and heat treated at 1220 and 1300 °C), e) and f), N6, N7, N8, N9 (HIPped at 1220 °C and heat treated at 1270 and 1200 °C, and HIPed at 1300 °C). Only FT moduli are shown.

Finally, the linear combination analysis of all Y K-edge XANES spectra has been performed using the data for the as-atomized powder (N3) and the sample consolidated by HIP at 1220 ºC followed by heat treatment at 1320 °C (N8) as standards. The result of the analysis is shown in Figure 16 and depicts the evolution of the oxidation degree of yttrium atoms from as-atomized powder to, HIPped and heat-treated samples.
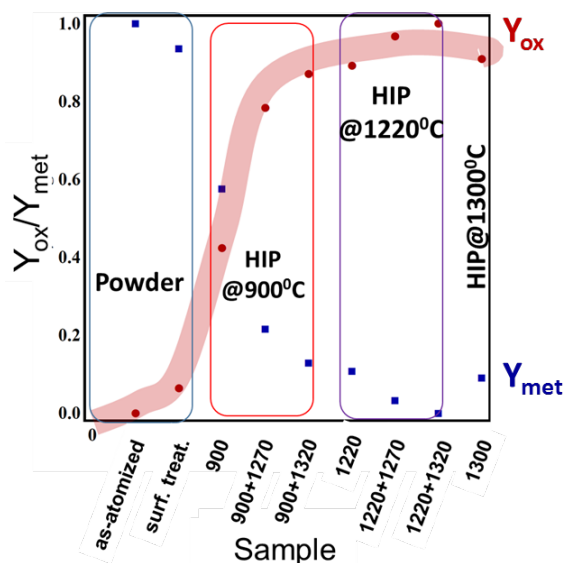

Figure 16. Linear combination analysis of the XANES spectra for all samples, using as-atomized powder (N3) and sample HIPped at 1220 °C + HT at 1320 °C (N8) as standards.

1.2. Ti K-edge spectra

The analysis of the Ti K-edge X-ray absorption spectra shows that the local structure of titanium has a different behaviour compared to that of yttrium. Based on the shape of the XANES and EXAFS spectra in Figure 17 the samples given in Table 2 can be divided into two main groups: the samples (N6-N9) HIPped at 1220 °C and heat-treated (at 1270 and 1320 °C), and the rest of the samples. The main differences between these two groups of samples is related to: (i) the Ti-Me peak at 2.2 Å in FTs, characteristic for titanium in steel matrix, and (ii) the Ti-O/C peak at 1.6 Å and satellite peak at 2.4-2.6 Å due to the Ti-O/C-Me bonds, characteristic of titanium oxide and carbide (1st and 2nd coordination

15

shells). Therefore, only samples (N6-N8) HIPped at 1220 °C and heat-treated show clear signs of titanium oxidation, whereas all other samples mimic titanium in metal matrix.

In particular, in the case of the as atomized powder N1, its XANES and FT of EXAFS are close to main characteristic features (edge position and the peak at 2.0-2.4 Å) of titanium foil (Figure 17a and b). Note that when titanium is coordinated by oxygen atoms as in the reference compounds TiO, Ti_2O_3 and rutile TiO_2, the chemical shift of the X-ray absorption edge occurs due to an increase of the effective positive charge on titanium ions and the peak at about 1.5 Å appears due to the Ti-O bonds.

The samples N3-N5 HIPed at 900 °C after heat treatment (Figure 17c and d) undergo an enhancement of the existing features. Some increase of the FT peaks can be a sign of the disorder decrease in the local structure around titanium atoms.

More substantial changes in the titanium local structure occur during heat treatment of samples N6-N8 HIPped at 1220 °C (Figure 17e and f). The peak at 2.2 Å, corresponding to the Ti-Me distance for metallic titanium in steel matrix, disappears with post-HIP heat treatments. Simultaneously, two peaks corresponding to Ti-O bonds at 1.6 Å and Ti-O-Me at 2.4-2.6 Å are developed. This is a strong indicator that the majority of titanium is oxidized after the heat treatment.

It is important to note that all samples may also contain fractions of TiC/N/O (carbides, nitrides, oxides). Quantitative analysis of XAS spectra at current stage is not possible, since the measured signal contains a superposition of many contributions and also significant amount of noise. The use of additional reference materials (for example, metallic Ti in iron matrix, TiN/C nanoparticles) could contribute positively into more accurate qualitative analysis of available XAS data and is planned in the future.
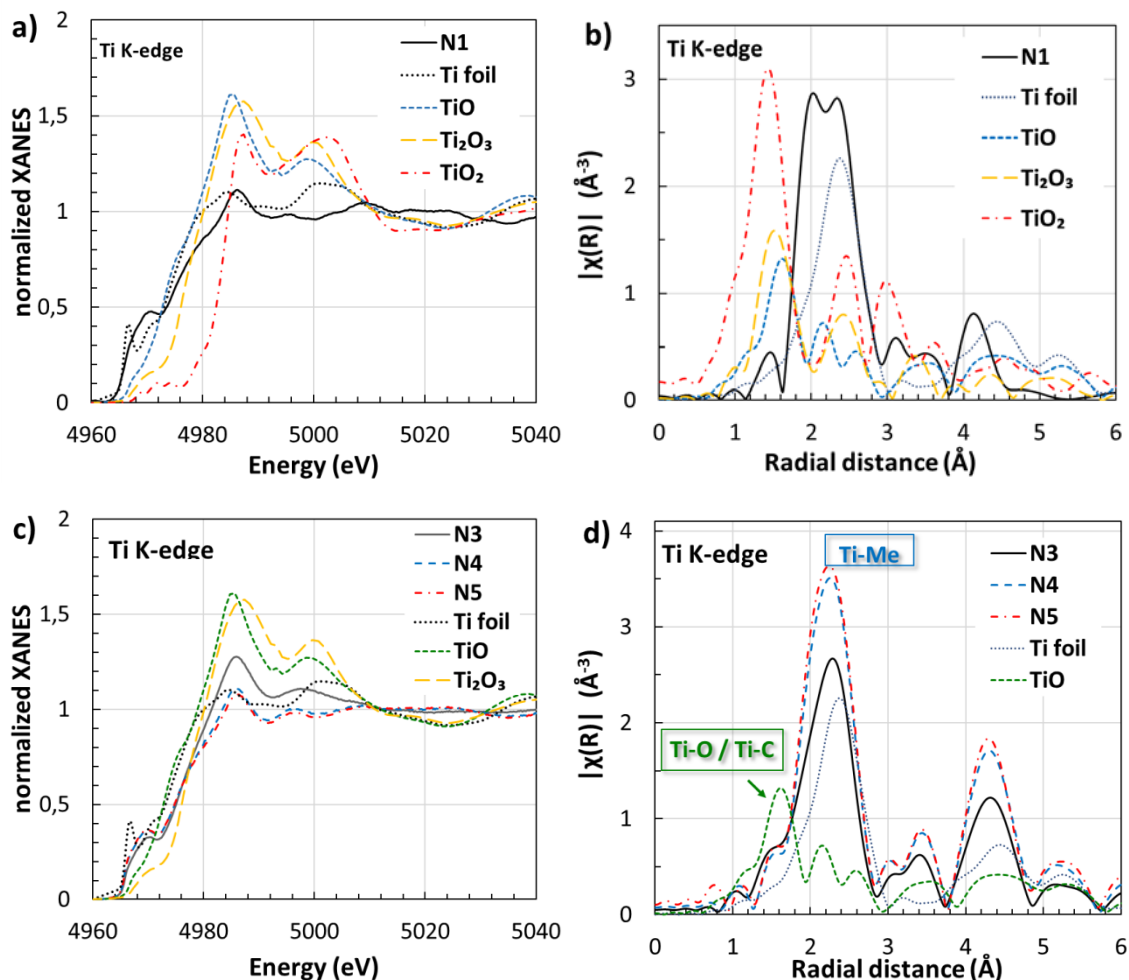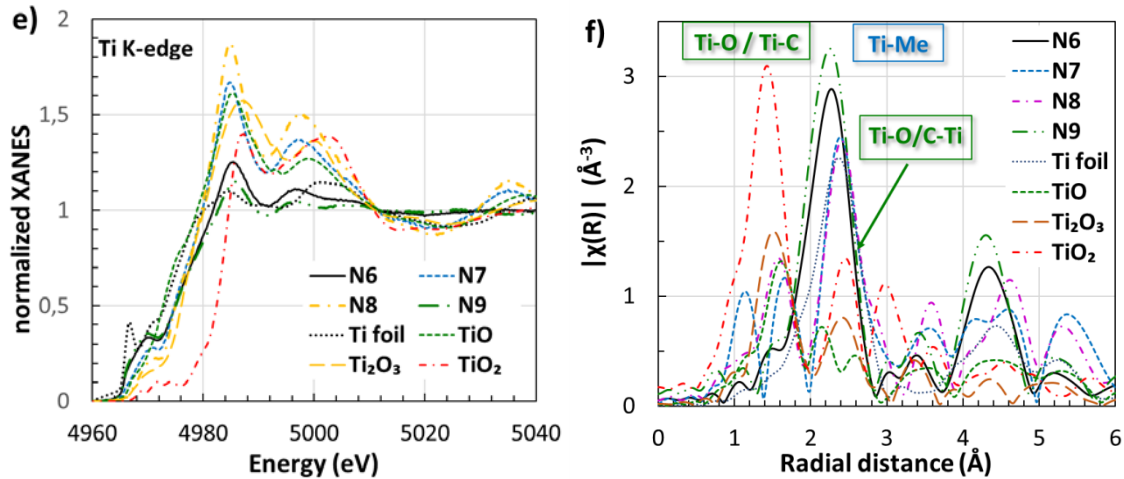
Figure 17. Ti K-edge XANES (a, c and e) and Fourier transforms (FTs) of EXAFS (b, d and f) for analyzed samples and references (Ti foil, TiO, TiO_2 and Y_2TiO_5. a) and b), N1 (as-atomized powder); c) and d), N3, N4 and N5 (HIPped at 900 ºC and heat treated at 1220 and 1300 °C), e) and f), N6, N7, N8, N9 (HIPped at 1220 °C and heat treated at 1270 and 1320 ºC, and HIPed at 1300 °C). Only FT moduli are shown.

2. Discussion

The formation of less thermodynamically stable oxides (Fe_2O_3, FeO and Cr_2O_3) at the surface of powder particles takes place under controlled parameters of heat treatment of the gas atomized powders, under oxidizing atmosphere. Yttrium at the most superficial layer is also oxidized (Figure 4b) to a depth of few nanometers, remaining the majority of this element metallic, both in the as-atomized and oxidized powder, as XAS analysis has demonstrated. The oxygen introduced during the oxidation acts as a reservoir to form, during consolidation at high temperature, a dispersion of more thermodynamically stable nanometric oxides, as it is described below.

During consolidation by HIP the initial metastable Fe_2O_3, FeO and Cr_2O_3 oxides are trapped along the PPBs (Figure 5a and b), and remain there until the material reaches temperatures high enough to promote their dissociation (Figure 5c, and Figure 6a and c). The oxygen from the dissociated oxides diffuses away from the PPBs towards the interior of powder particles, where the oxygen concentration is very low, between 50 and 80 ppm [17], and reacts with Y (and Ti or Al) to form more thermodynamically stable nanometric oxides (Figure 5d, Figure 6e and f, Figure 9, Figure 12). This oxygen exchange occurs until one of these situations takes place: the metastable oxides at PPBs are fully dissociated, or no more metallic Y remains in the ferritic grains.

Therefore, distribution of Y during solidification of atomized particles is a key aspect controlling the homogeneity in which nanometric oxides are distributed in the ferritic matrix. In this sense, finer powders (<20 µm), that solidify and cool at higher solidification rates allow reducing and even avoiding Y migration and segregation at grain boundaries [20] and, therefore, lead to finer oxides. However, since the yield of fine powders during atomization is very low (about 10% for particles below 20 µm) the work shown here corresponds to powders with particle size ranging from 20 to 45 µm.

Samples consolidated at low temperature, 900 °C, provide information about the oxidation of the alloying elements in an intermediate state: whereas iron oxides are probably fully dissociated, and only a residual fraction of Cr_2O_3 remains at PPBs, a small fraction of Y and Ti (and Al from contamination) has diffused towards PPBs and is oxidized. SEM observations confirm the dissociation of iron oxide and the presence of chromium oxide at the PPBs (Figure 5b). In addition, Ti-, Y- and Al-enrichment was also observed at PPBs, supporting the hypothesis of partial dissociation of metastable oxides to form more stable Ti-, Y- and Al-rich oxides. Inside PPBs, Y oversaturated in the ferritic grains precipitates as a submicrometric non oxidized Y-rich phase, which also contains W. The metallic nature of the Y constituting these intermetallic (Y,W)-rich particles inside PBBs, and the oxidation of yttrium at PPBs has been supported

17

by XAS (Figure 14 c and d and Figure 15). Ti remains metallic, dissolved in the ferritic grains. The heat treatments performed at high temperature after this low-temperature HIP result in almost complete dissociation of oxides at PPBs, coarsening of Y- and Ti-rich particles at PPBs (Figure 5e, precipitates 1 and 3) and also in the precipitation of fine nanometric Y-rich oxides (probably Y_2O_3) (finest precipitates in Figure 5e, for example number 2). However, and according to XAS analysis, these heat treatments do not lead to complete oxidation of neither yttrium (Figure 16) nor titanium (Figure 17c and d). In addition, the absence of a suitable population of highly stable nanoparticles promotes during post-HIP heat treatments after HIPping at low temperature (*Table 3*). Therefore, the route consisting of HIPping at low temperature (900 °C) followed by heat treating at high temperatures (1220 °C and 1300 °C), does not completely exploit the potential of the oxide formers introduced during atomization, and should be discarded to obtain ODS steels following the STARS route.

The microstructure observed after HIP consolidation at high temperature, above 1200ºC is similar to that obtained after HIPping at low temperature and additional heat treating: metastable oxides at PPBs are completely dissociated (Figure 6a and c) and, although some Y- and Ti-rich submicrometric particles are observed at PPBs and grain or subgrain boundaries, a profuse precipitation of nanometric oxides is observed inside grains, preferentially in the vicinity of boundaries (Figure 6b and d and Figure 7). However, XAS analysis reveals relevant differences, which are related to the mechanisms by which the oxide nanoparticles are formed:

- The overall oxidation degree of Y is higher after HIPping at high temperature (Figure 16), regardless of whether a post-HIP heat treatment is performed.

- Only after consolidation by HIP at high temperature and subsequent heat treatment titanium is significantly oxidized (Figure 17 e and f).

- Despite Y_2TiO_5 nanoparticles were found by TEM (Figure 9a and b), from XAS analysis titanium is mostly metallic, suggesting that, in order to increase the number density of nanoparticles, certain parameters of the STARS route need further optimization.

Aluminium, present as a non-desired contamination introduced during atomization, plays a key role during the precipitation of the oxide nanoparticles. Due to the higher enthalpy formation of alumina (-1675,7 kJ/mol)[35] than titania (-945 KJ/mol) [36], the oxygen from the metastable oxides dissociated during HIPping tends to preferentially combine with aluminium rather than titanium and, as a final result, both elements compete to react with oxygen. The peaks in the FTs of EXAFS of Y after HIPping and post-HIP heat-treating attributed to Y-Me-O (Figure 14d and f) probably correspond to both Y-Al-O and Y-Ti-O oxides, whose presence has been confirmed by HRTEM as $Y_4Al_2O_9$ and Y_2TiO_5 nanoparticles (Figure 9 and Figure 12). Consequently, it can be confirmed that aluminium contamination hinders precipitation of Y_2TiO_5 nanoparticles, and both Y_2TiO_5 and $Y_4Al_2O_9$ nanoparticles form. The small aluminium additions are known to coarsen the oxide nanoparticles and degrade the high temperature strength of ODS alloys [37], and need to be drastically reduced. The presence of Ti that remains unonxidized at PPBs and grain or sub-grain boundaries, probably forming Ti(C,N), has been confirmed by XAS (Figure 17f).

3. Conclusions

The mechanism proposed in the STARS route by which ODS FS can be obtained without MA has been demonstrated:

- It has been confirmed that after atomization yttrium remains metallic inside powder particles forming intermetallics whose thermal stability is low enough to decompose during consolidation by HIP. Therefore, these Y-rich intermetallics act as yttrium reservoir to form nanometric thermodynamically oxides during consolidation at high temperature (as high as 1220 °C).

- The presence of a metastable oxide nano-layer at the surface of powder particles has been confirmed, this layer acts as oxygen reservoir that dissociates gradually during consolidation by HIP to form a nanometric oxide dispersion

- XAS analyses have evidenced that consolidation at elevated temperatures (and subsequent heat treatment) promotes oxygen exchange between the metastable oxides at PPBs and the Y-rich intemetallic, present inside ferritic grains during intermediate stages of HIP.

- Microstructural analysis of samples consolidated at high temperature (1220 and 1300 °C) reveals the almost complete dissolution of the metastable oxides at PPBs and the precipitation of highly stable nanoparticles, identified as $Y_4Al_2O_9$ and Y_2TiO_5 by TEM .

Contamination with Al has a negative impact on microstructure, promoting the precipitation of $Y_4Al_2O_9$, in addition to Y_2TiO_5. A reduction from 800 to 200-300 ppm in Al content is expected to have a strong beneficial effect on final microstructure and behaviour.

HIP at low temperature (900°C) is not effective in achieving the desired nanometric Ti-Y-O oxides, because it only leads to partial oxidation of Y. Since additional heat treatments at high temperatures (1220 and 1300 ºC) do not promote oxidation of Ti to form complex nanometric oxides and cause growth of ferritic grains and development of TIP, this consolidation route is discarded.

References

[1]. S. J. Zinkle and J.T. Busby, Structural Materials for fission and fusion energy. Materials Today, vol. 12 (2009), pp.12-18

[2]. N. Baluc et al., Review on the EFDA work programme on nano-structured ODS RAF steels, Journal of Nuclear Materials, vol. 417 (2011),pp. 149–153.

[3]. G.R. Odette, Recent progress in developing and qualifying nanostructured ferritic alloys for advanced fission and fusion applications. Journal of the Minerals, Metals and Materials Society, vol 66 (2014), pp. 2427-2441

[4]. S. J. Zinkle et al., Development of next generation tempered and ODS reduced activation ferritic/martensitic steels for fusion energy applications. Nuclear Fusion 57 (2017), pp. 092005-092021.

[5]. G. R. Odette. On the status and prospects for nanostructured ferritic alloys for nuclear fission and fusion application with emphasis on the underlying science. Scripta Materialia, in press, 2017

[6]. A. Hirata et al., Atomic structure of nanoclusters in oxide-dispersion-strengthened steels, Nature Materials, vol. 10 (2011), pp. 922-926.

[7]. J. Hurley, Applications for Dispersion-Strengthened Alloys in Thermal Power Systems. Proceedings of the Twenty Fisrt Annual Conference On Fossil Energy Materials, Knoxville, Tennessee, 2007, pp 29-37.

[8]. D. T. Hoelzer, J. Bentley, M. A. Sokolov, M. K. Miller, G. R. Odette, and M. J. Alinger, Influence of particle dispersions on the high-temperature strength of ferritic alloys, Journal of Nuclear Materials, 367–370 (2007), 166–172.

[9]. D. A. McClintock, D. T. Hoelzer, M. A. Sokolov, and R. K. Nanstad, Mechanical properties of neutron irradiated nanostructured ferritic alloy 14YWT, Journal of Nuclear Materials, 386–388 (2009), 307–311.

[10]. D. T. Hoelzer et al., Influence of processing on the microstructure and mechanical properties of 14YWT. Journal of Nuclear Materials 471 (2016), 251-265.

[11]. Z. Oksiuta et al., Mechanical properties and thermal stability of nanostructured ODS RAF steels, Mechanics of Materials, 67 (2013), 15-24

[12]. Y. Sawazaki et al., Development of 15CrODS ferritic steels for over 1273 K service. Journal of Nuclear Materials 442 (2013), pp. S169-S172

[13]. J.P. Wharry, M.J. Swenson, and K.H. Yano. A review of the irradiation evolution of dispersed oxide nanoparticles in b.c.c. Fe-Cr alloys: current understanding and future directions. Journal of Nuclear Materials, vol. 486 (2017), pp. 11-20

[14]. E. Aydogan et al., Stability of nanosized oxides in ferrite under extremely high dose self ion irradiations. Journal of Nuclear Materials 486 (2017), pp 86-95

[15]. M. Ratti et al. Influence of titanium on nano-cluster (Y, Ti, O) stability in ODS ferritic materials, Journal of Nuclear Materials, vol. 386–388 (2009), pp. 540–543.

[16]. E. Gil et al. Microstructural characterization of ODS ferritic steels at different processing stages, Fusion Engineering and Design, vol. 98–99 (2015), pp. 1973–1977.

[17]. E. Gil et al. ODS ferritic steels produced by an alternative route (STARS): microstructural characterisation after atomisation, HIPping and heat treatments, Powder Metallurgy, vol. 59 (2016), pp. 359-369.

[18]. E. Gil et al., XPS and SEM analysis of the surface of gas atomized powder precursor of ODS ferritic steels obtained through the STARS route, Applied Surface Science, vol. 427 (2018), pp. 182-191.

[19]. J. R. Rieken et al. Reactive gas atomization processing for Fe-based ODS alloys, Journal of Nuclear Materials, vol. 428 (2012), pp. 65–75.

[20]. J. R. Rieken., Gas atomized precursor alloy powder for oxide dispersion strengthened ferritic stainless steel, Ph.D. Thesis, Iowa State University, 2011.

[21]. P. He et al., XAFS and TEM studies of the structural evolution of yttrium-enriched oxides in nanostructured ferritic alloys fabricated by powder metallurgy process. Materials Chemistry and Physics 136 (2012), pp. 990-998

[22]. S. Liu, et. al., Evidence for core-shell nanoclusters in oxygen dispersion strengthened steels measured using X-ray absorption spectroscopy., Journal of Nuclear Materials vol. 445 (2014) pp.50-56.

[23]. T. Malis, S.C. Cheng and R.F. Egerton, Journal of Electronic Microscopy Techonologies, vol. 8 (1988), pp. 193–200.

[24]. S. Belin et al. SAMBA a new beamline at SOLEIL for x-ray absorption spectroscopy in the 4-40 keV energy range, Physica Scripta, vol. T115 (2005), vol. 980-983.

[25]. V.L. Aksenov, et al. EXAFS spectroscopy at synchrotron-radiation beams, Physics of Particles and Nuclei, vol. 32 (2001), pp. 675-707.

[26]. A. Kuzmin. EDA: EXAFS data analysis software package, Physica B 208-209 (1995) 175-176.

[27]. B. Ravel and M. Newville. ATHENA, ARTEMIS, HEPHAESTUS: data analysis for X-ray absorption spectroscopy using IFEFFIT, Journal of Synchrotron Radiation, vol. 12 (2005), pp. 537–541.

[28]. A.L. Ankudinov et al. Real Space Multiple Scattering Calculation of XANES, Physical Revew. B, vol. 58 (1998), p. 7565.

[29]. A. Cintins et a. ODS steel raw material local structure analysis using X-ray absorption spectroscopy, IOP Conference Series: Materials Science and Engineering, vol. 77 (2015) pp. 012029-012034.

[30]. M.S. Farkas and A.A. Bauer. The solid solubility and constitution of yttrium in iron-20 to 40 w/o chromium alloys, Technical report (BMI-1386), Battelle Memorial Inst., Columbus, Ohio, 1959.

[31]. S. G. Epstein, A.A. Bauer, and R.F. Dickerson. Solubility limits of yttrium and the lanthanide rare-earth elements in chromium and chromium-rion alloys, Technical report (BMI-1376), Battelle Memorial Inst., Culumbus, Ohio, 1959.

[32]. A. Certain et al. Radiation stability of nanoclusters in nano-structured oxide dispersion strengthened. (ODS) steels, Journal of Nuclear Materials, vol. 434 (2013), pp. 311–321.

[33]. J. Macías-Delgado et al., Microstructure and tensile properties of ODS ferritic steels mechanically alloyed with Fe_2Y, Nuclear Materials and Energy, vol. 9 (2016), pp. 372–377.

[34]. M. Laurent-Brocq et al., Inluence of ball-milling and annealing conditions on nanocluster characteristics in oxide dispersion strengthened steels, Acta Materialia, vol. 60, (2012), pp 7150-7159.

[35]. D. Ghosh and D. A. R. Kay. Standard free energy formation of alumina, Journal of the Electrochemcial Society, vol. 124 (1977), pp 1836-1845.

[36]. S. Zumdahl, Chemical Principles 6th Ed. Houghton Mifflin Company (2009), p. A23

[37]. S. Ohtsuka et al. Effects of aluminum on high-temperature strength of 9Cr-ODS steel, Journal of Nuclear Materials, vol. 386-388 (2009), pp. 479-482.